

Supporting Information

High Performance of Potassium Poly(heptazine imide) Films for Photoelectrochemical Water Splitting

Xiaochun Li, Xiaoxiao Chen, Yuanxing Fang,* Wei Lin, Yalong Hou, Masakazu Anpo,

Xianzhi Fu and Xinchun Wang*

State Key Laboratory of Photocatalysis on Energy and Environment, College of Chemistry,

Fuzhou University, Fuzhou 350116, P. R. China

Email: yxfang@fzu.edu.cn; xcwang@fzu.edu.cn

Contents

Figure S1. Illustration of experimental procedures for the synthesis of K-PHI films based photoanode.	1
Figure S2. SEM images of the of (a, b) melon and (c, d) K-PHI.	2
Figure S3. SEM images of the cross-sectional views of (a) melon and (b) K-PHI.	3
Figure S4. (a) TEM and (b) High-resolution TEM images of melon.	3
Figure S5. SAED patterns of K-PHI.	4
Figure S6. TEM images of SnS ₂ in K-PHI films.	4
Figure S7. TEM accompanied with EDS technique to study the elements of (a) tin and (b) sulfur.	5
Figure S8. EDS results of the K-PHI films and the detail of the elemental analysis, including atomic fraction, mass fraction.	6
Figure S9. XRD spectra of melon and K-PHI. The peaks at 15°, 28.2°, 32.1° and 49.9° can be attributed to SnS ₂ (JCPDS No. 22-0951).	7
Figure S10. Kubelka-Munk plots of (a) melon and (b) K-PHI. Both materials were considered as direct bandgap.	8
Figure S11. Digital photograph of melon and K-PHI based photoanodes.	8
Figure S12. Mott-Schottky plots of (a) melon and (b) K-PHI to measure the flat-band potentials.	9
Figure S13. Band structure of Melon and K-PHI.	9
Figure S14. (a) Structure model of melon. (b) Calculated band structure and (c) corresponding PDOS for melon.	10
Figure S15. The orbital diagrams of (a) CBM and (b) VBM of PHI. The orbitals with cyan and yellow colours represent the positive and negative values of the molecular orbitals. The pink, brown and gray balls represent H, C and N atoms, respectively.	11
Figure S16. The photocurrent density of the K-PHI photoanode in the electrolyte solution with certain concentration of NaOH, and the measurements were conducted at the voltage of 1.23 V vs. RHE under AM 1.5G illumination.	12
Figure S17. Photocurrent densities of K-PHI and 2.65 at% SnS ₂ /K-PHI powder-based photoanodes in 1.0 M NaOH aqueous solution at voltage of 1.23 V vs. RHE under AM 1.5G illumination.	12
Figure S18. The sheet resistance of the FTO layer and the exposed SnS ₂ /FTO layer by scraping off the films measured by a a four-point probe.	13
Figure S19. An hour measurement of K-PHI photoanode for water splitting under 1.23 V vs. RHE in 1.0 M NaOH under AM 1.5G illumination.	13
Figure S20. SEM images of K-PHI (a, b) before and (c, d) after an hour water splitting reaction.	14
Figure S21. (a) XRD spectra and high-resolution XPS spectra of (b) K 2 <i>p</i> , C 1 <i>s</i> , (c) N 1 <i>s</i> , (d) S 2 <i>p</i> , (e) Sn 3 <i>d</i> and (f) O 1 <i>s</i> of K-PHI before and after an hour water splitting reaction.	14
Figure S22. (a) Photocurrent density of K-PHI at voltage of 1.23 V vs. RHE under AM 1.5G illumination. (b) The evolved gas is collected to analyze by gas chromatography. Inset: the corresponding magnificent signals. The first, second and third peaks stands hydrogen, oxygen and nitrogen gases.	15
Figure S23. ABPE of melon and K-PHI calculated from LSV curves in 1.0 M NaOH aqueous solution. ..	15
Figure S24. PL spectra of melon and K-PHI.	16
Figure S25. (a) Nyquist plots of melon and K-PHI photoanode (a) without and (b) with AM 1.5G illumination, and equivalent circuits are shown in the corresponding insets. (c) The fitting of the impedance spectrum.	17

Figure S26. IMPS response of amorphous melon based photoanode.	18
Table S1. Summary of PEC performance of this work and the reported PCN-based photoanodes.	19
Reference	23

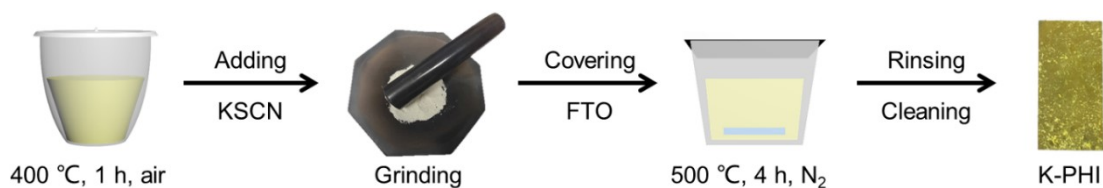


Figure S1. Illustration of experimental procedures for the synthesis of K-PHI films based photoanode.

Discussion

Melamine was pre-heated for partially polymerization to form heptazine. The prepared powder was blended with KSCN to a homogeneous mixture. The mixture was transferred into a crucible and a clean FTO was embedded into the precursor. After thermal treatment in the nitrogen gas atmosphere, the films would grow on the substrate. Residue should be washed prior to PEC water splitting.

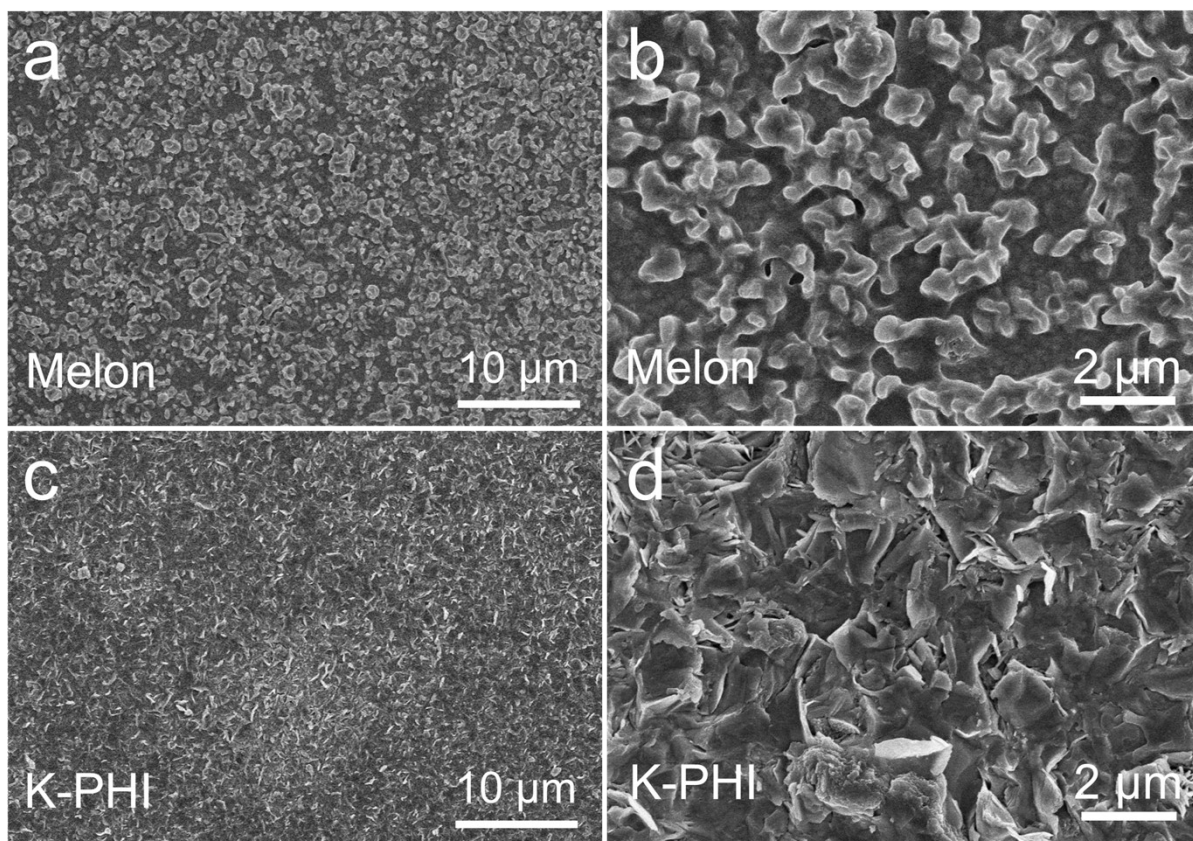


Figure S2. SEM images of the of (a, b) melon and (c, d) K-PHI.

Discussion

The morphologies of melon and K-PHI are homogeneous, and their difference can be clearly realized. The melon films are soft as shown in Figure **S2a** and **S2b**, and K-PHI films are relatively rigid as shown in Figure **S2c** and **S2d**. These observations indicate the formation of the the K-PHI is formed with improved crystallinity.

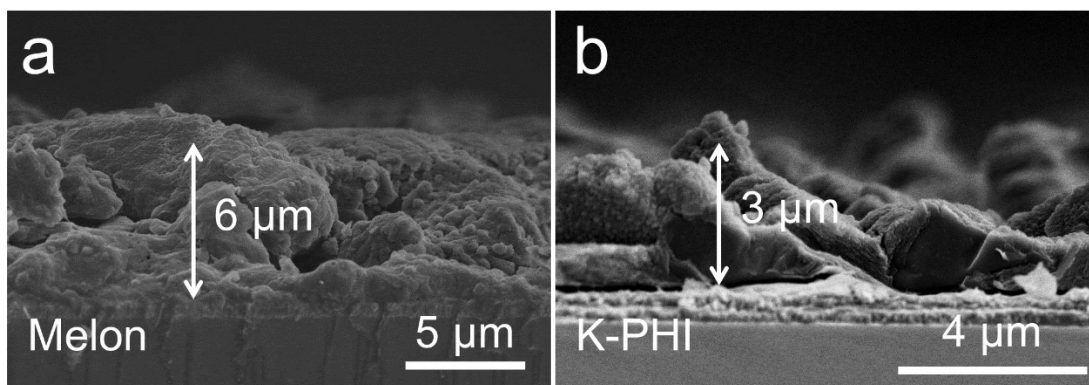


Figure S3. SEM images of the cross-sectional views of (a) melon and (b) K-PHI.

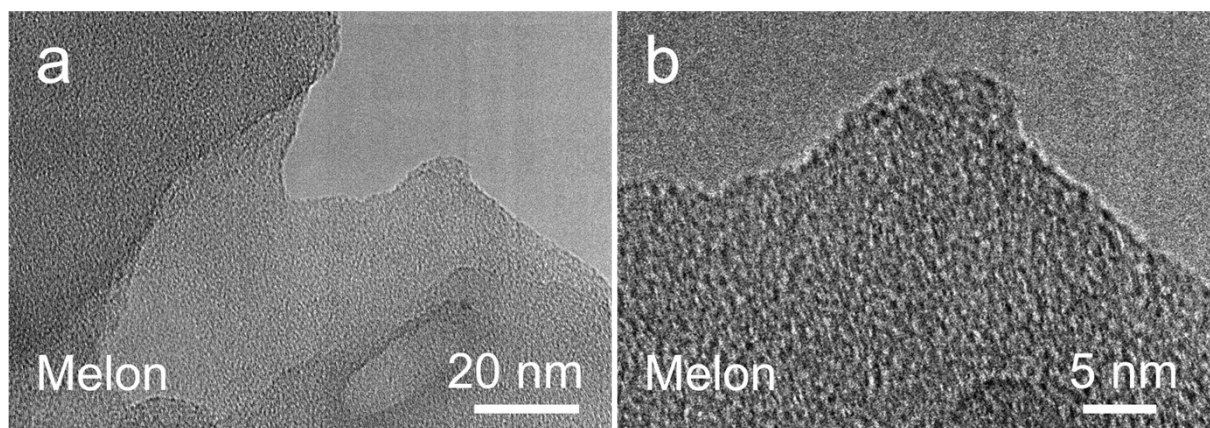


Figure S4. (a) TEM and (b) High-resolution TEM images of melon.

Discussion

The general thickness of the melon films is larger than K-PHI films in this case as shown in **Figure S3**, the mean thickness is ca. 6 μm, whereas K-PHI is ca. 3 μm. The rigid morphology of the K-PHI can be clearly observed from this cross-sectional view. The thicknesses of different K-PHI films are similar since the polymerization only occurs near the SnS₂. Compared with K-PHI films, it is rare to observe any lattice fringes from melon films in the TEM image as shown in **Figure S4**, and this fact reveals the crystallinity of melon is significantly low.

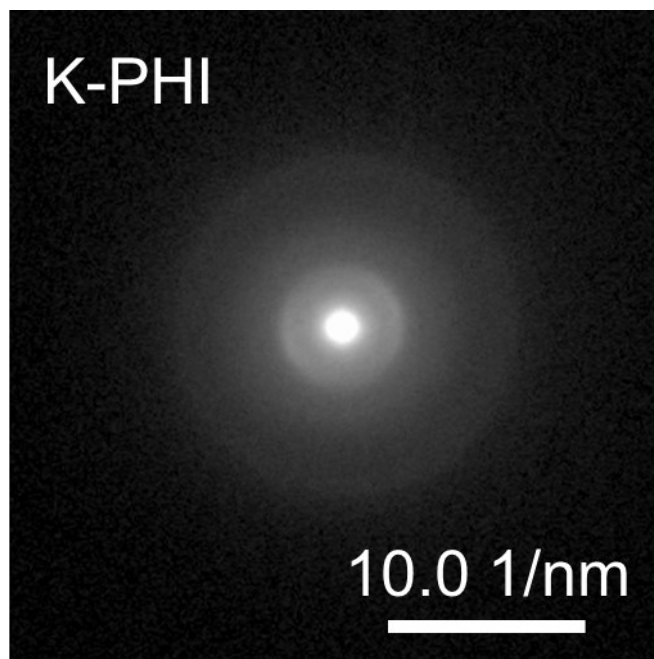


Figure S5. SAED patterns of K-PHI.

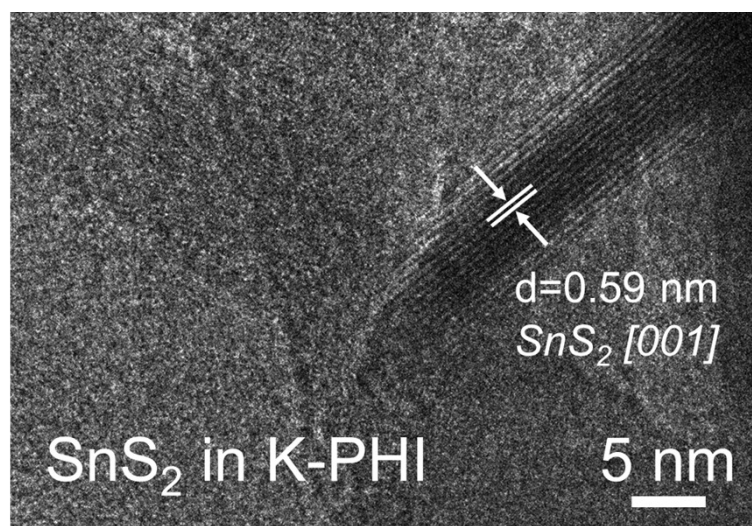


Figure S6. TEM images of SnS₂ in K-PHI films.

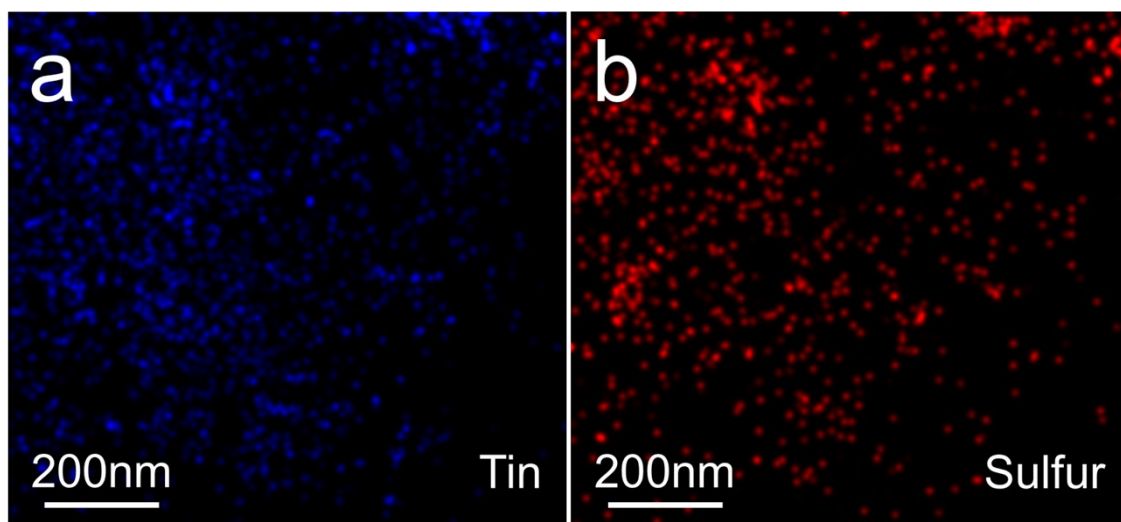
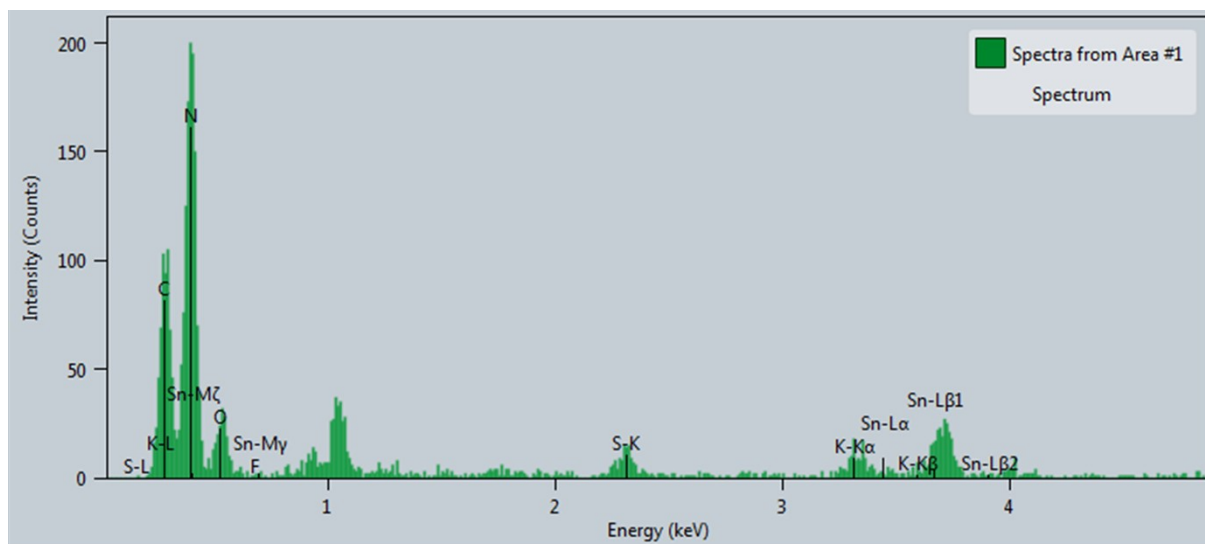


Figure S7. TEM accompanied with EDS technique to study the elements of (a) tin and (b) sulfur.



Z	Element	Family	Atomic Fraction (%)	Atomic Error (%)	Mass Fraction (%)	Mass Error (%)	Fit error (%)
6	C	K	37.68	8.57	30.93	4.74	9.22
7	N	K	52.36	15.40	49.11	11.85	5.75
8	O	K	5.70	1.66	6.35	1.51	3.46
9	F	K	0.00	0.32	0.00	0.38	0.00
16	S	K	1.79	0.51	3.72	0.85	4.77
19	K	K	1.61	0.45	3.78	0.83	4.88
50	Sn	K	0.86	0.84	6.10	5.89	99.36

Figure S8. EDS results of the K-PHI films and the detail of the elemental analysis, including atomic fraction, mass fraction.

Discussion

Figure S6 to S8 study the SnS_2 among K-PHI. In **Figure S6**, we can clearly observe SnS_2 among K-PHI films in the TEM image. The lattice fringes of 0.59 nm are attributed to the [001] crystal facets of SnS_2 . In **Figure S7**, the TEM accompanied with EDS investigation has presented distribution of the Sn and S element among the K-PHI films, and this result indicates a low concentration of SnS_2 among the films. A quantitative analysis of EDS results is shown in **Figure S8**. We can calculate the atomic percentage of SnS_2 is only 2.65%, while the atomic percentage of carbon and nitride elements can be calculated to be ca. 90.04%, revealing carbon nitride polymer is the main composition of the films.

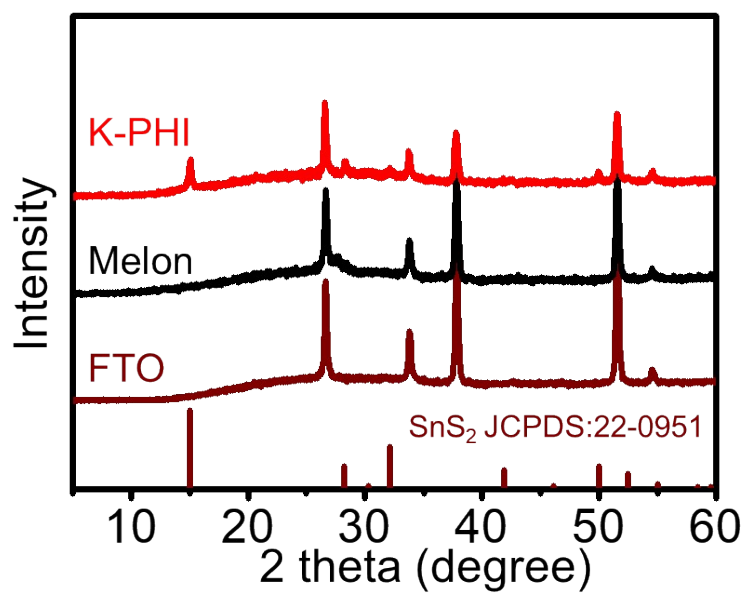


Figure S9. XRD spectra of melon and K-PHI. The peaks at 15°, 28.2°, 32.1° and 49.9° can be attributed to SnS₂ (JCPDS No. 22-0951).

Discussion

The domain peaks at 28.1° of K-PHI is overlapped with the SnS₂ peak, therefore in XRD spectra, it is difficult to distinguish the formation of the K-PHI in this case.

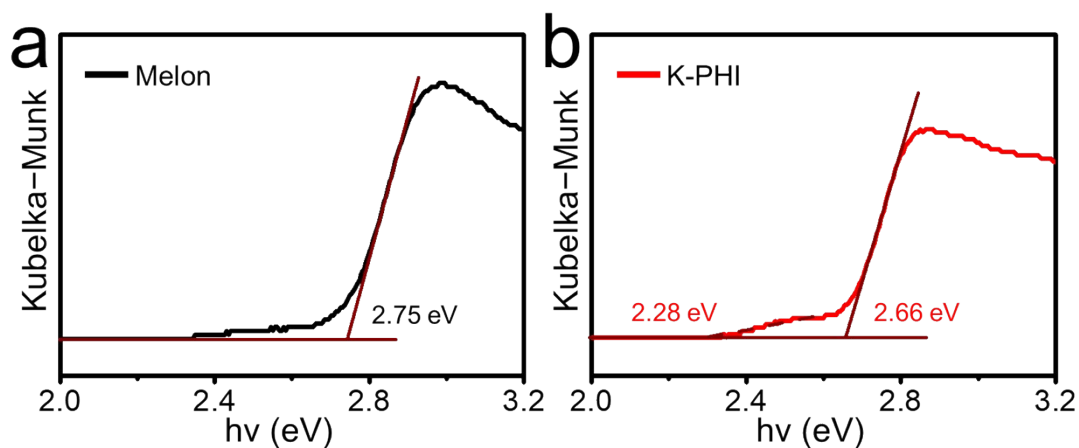


Figure S10. Kubelka-Munk plots of (a) melon and (b) K-PHI. Both materials were considered as direct bandgap.

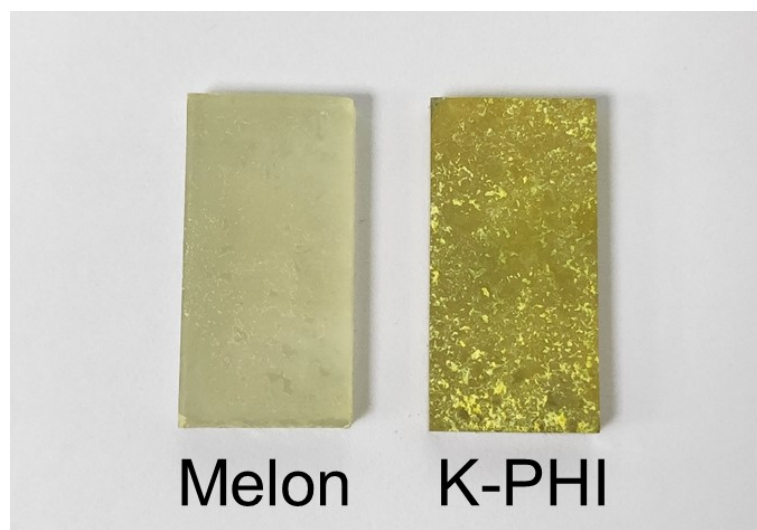


Figure S11. Digital photograph of melon and K-PHI based photoanodes.

Discussion

Figure S10 and **S11** show optical properties of the melon and K-PHI photoanode. In **Figure S10**, we can observe that the bandgap of K-PHI is smaller than melon, indicating the improved polymerization and crystallization. In addition, an obvious absorption from K-PHI films can be detected, and this spectrum is owing to the SnS_2 . From the digital photographs in **Figure S11**, the difference of the color reflects the improved visible light absorption by K-PHI films.

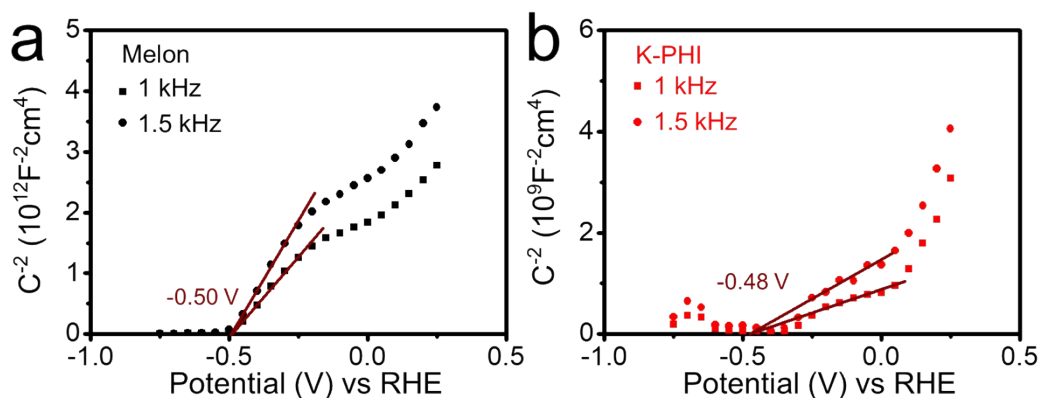


Figure S12. Mott-Schottky plots of (a) melon and (b) K-PHI to measure the flat-band potentials.

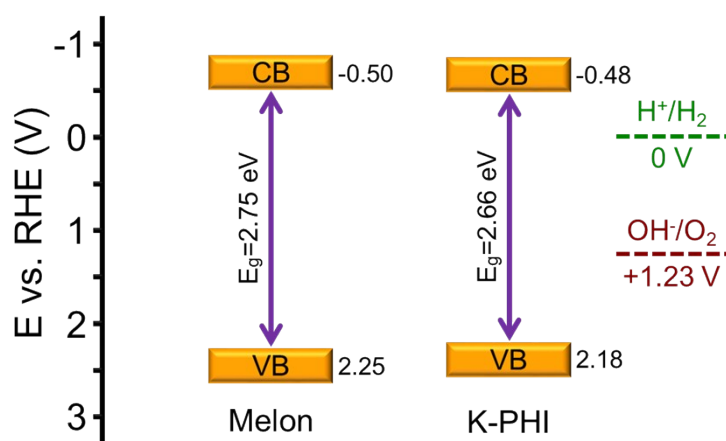


Figure S13. Band structure of Melon and K-PHI.

Discussion

Mott-Schottky plots of electrochemical impedance spectroscopy (EIS) is used to acquire the flat-band potential as shown in **Figure S12**. This flat-band potential highly relates to the conduction band and based on this result we can estimate the band structure as shown in **Figure S13**. Compared with melon material, the bandgap of K-PHI slightly shrinks owing to the improved polymerization and crystallization.

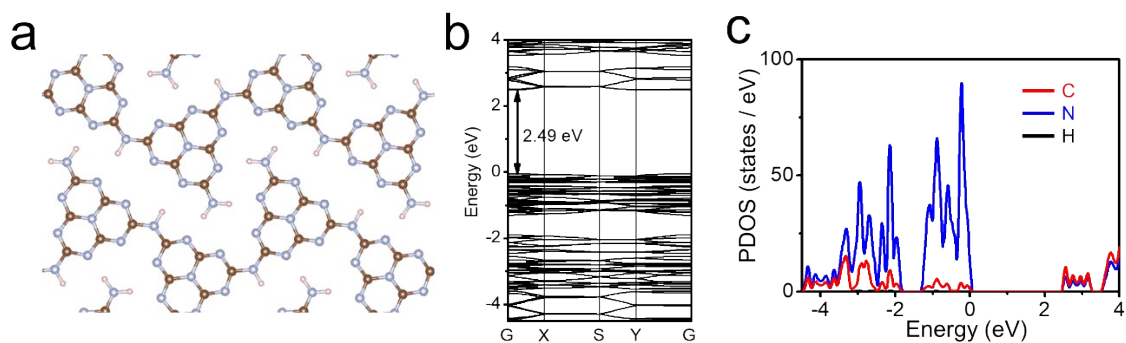


Figure S14. (a) Structure model of melon. (b) Calculated band structure and (c) corresponding PDOS for melon.

Discussion

We have conducted density functional theory (DFT) calculations to theoretical study the property of the melon. The structure model of melon is shown in **Figure S14**. The pink, brown and gray balls represent H, C and N atoms, respectively. Calculated band structure of melon is shown in **Figure S14b** and the corresponding projected density of states (PDOS) of melon is shown in **Figure S14c**. The bandgap of melon is larger than K-PHI, and the results make generally agreement with experimental studies.

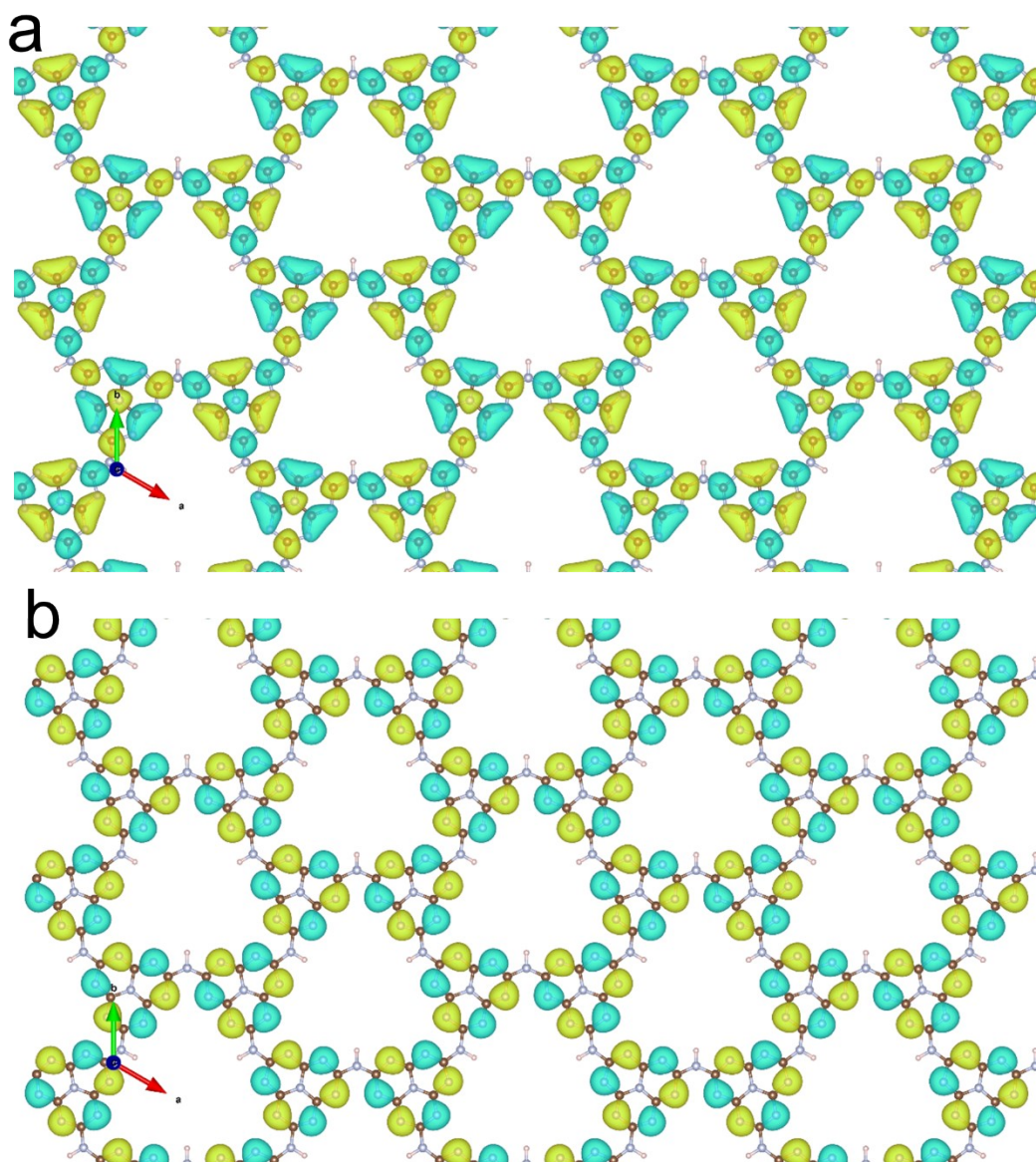


Figure S15. The orbital diagrams of (a) CBM and (b) VBM of PHI. The orbitals with cyan and yellow colours represent the positive and negative values of the molecular orbitals. The pink, brown and gray balls represent H, C and N atoms, respectively.

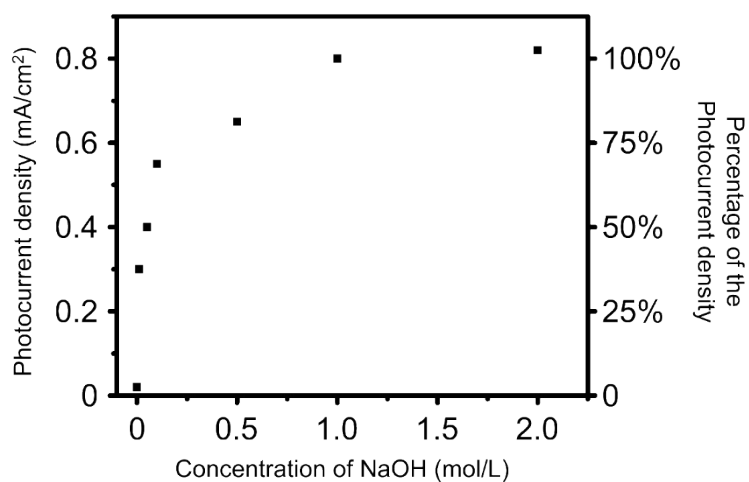


Figure S16. The photocurrent density of the K-PHI photoanode in the electrolyte solution with certain concentration of NaOH, and the measurements were conducted at the voltage of 1.23 V vs. RHE under AM 1.5G illumination.

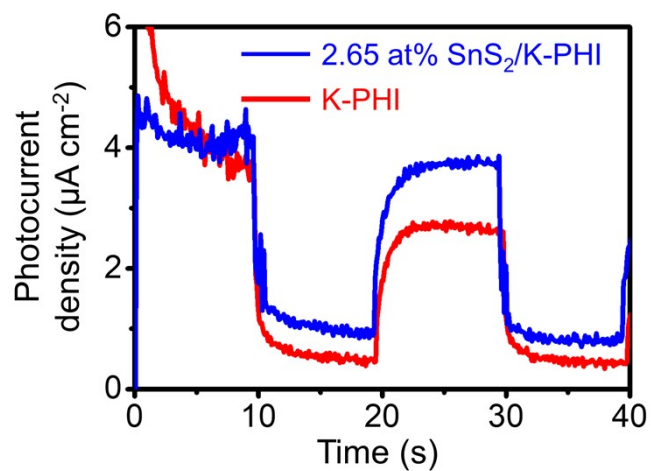


Figure S17. Photocurrent densities of K-PHI and 2.65 at% SnS₂/K-PHI powder-based photoanodes in 1.0 M NaOH aqueous solution at voltage of 1.23 V vs. RHE under AM 1.5G illumination.

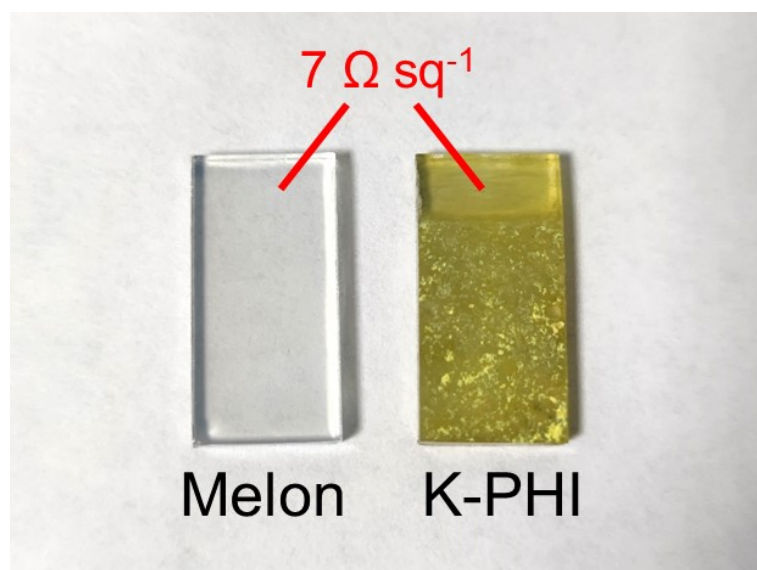


Figure S18. The sheet resistance of the FTO layer and the exposed SnS₂/FTO layer by scraping off the films measured by a four-point probe.

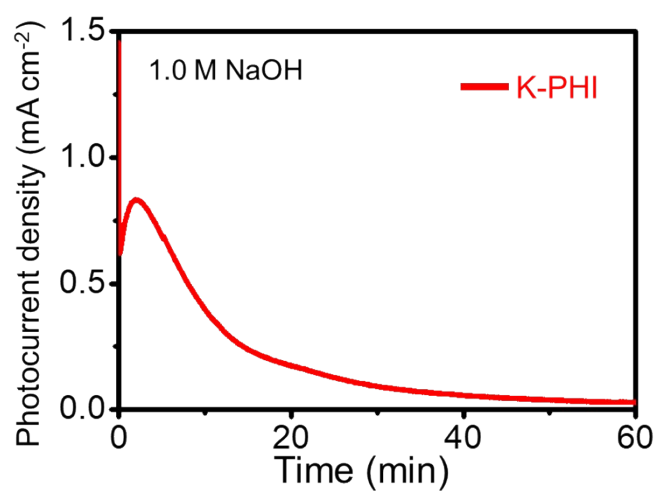


Figure S19. An hour measurement of K-PHI photoanode for water splitting under 1.23 V vs. RHE in 1.0 M NaOH under AM 1.5G illumination.

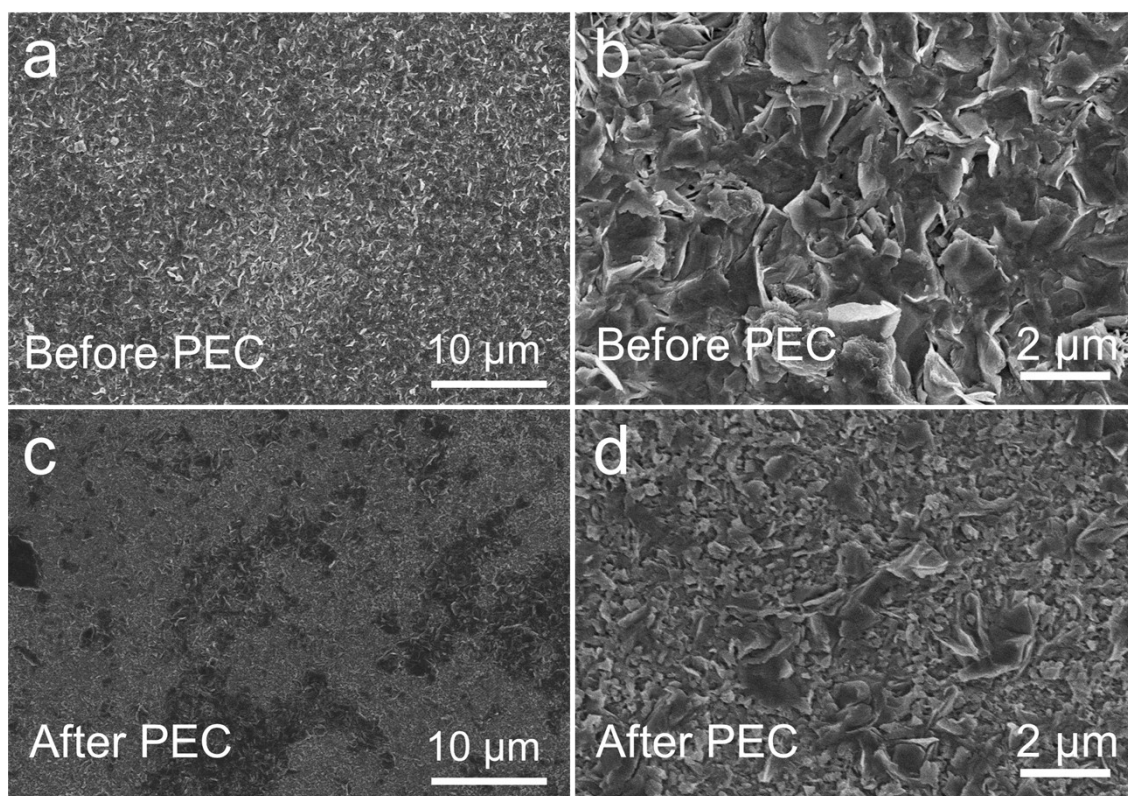


Figure S20. SEM images of K-PHI (a, b) before and (c, d) after an hour water splitting reaction.

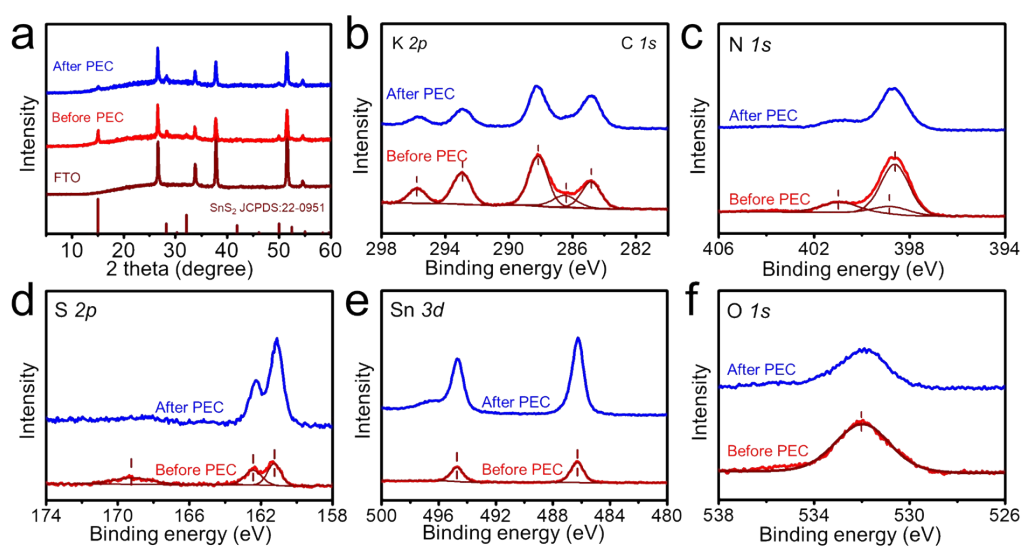


Figure S21. (a) XRD spectra and high-resolution XPS spectra of (b) K $2p$, C $1s$, (c) N $1s$, (d) S $2p$, (e) Sn $3d$ and (f) O $1s$ of K-PHI before and after an hour water splitting reaction.

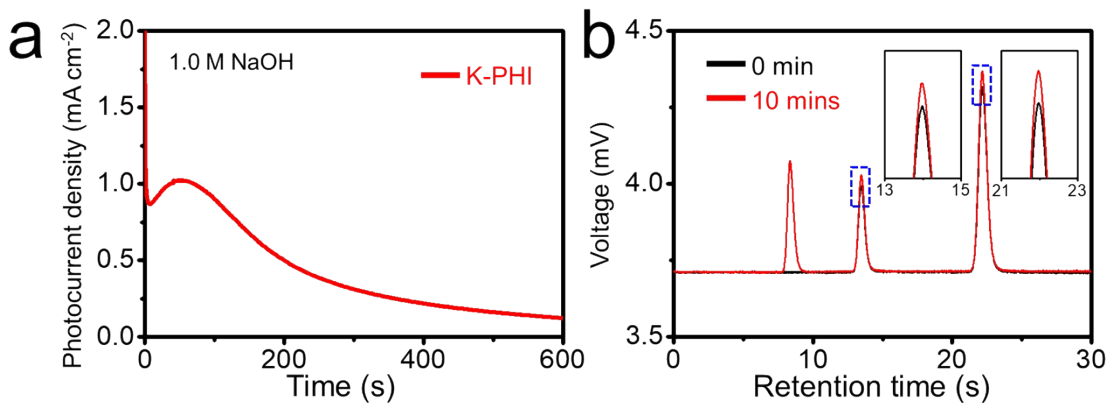


Figure S22. (a) Photocurrent density of K-PHI at voltage of 1.23 V vs. RHE under AM 1.5G illumination. (b) The evolved gas is collected to analyze by gas chromatography. Inset: the corresponding magnificent signals. The first, second and third peaks stands hydrogen, oxygen and nitrogen gases.

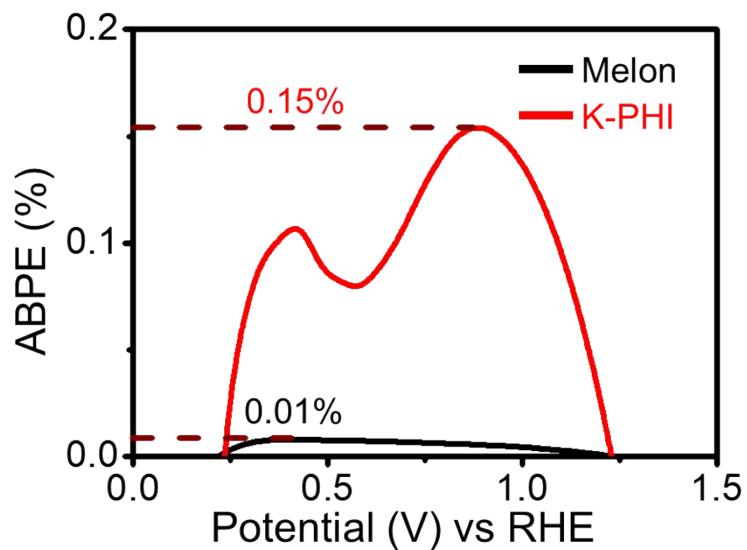


Figure S23. ABPE of melon and K-PHI calculated from LSV curves in 1.0 M NaOH aqueous solution.

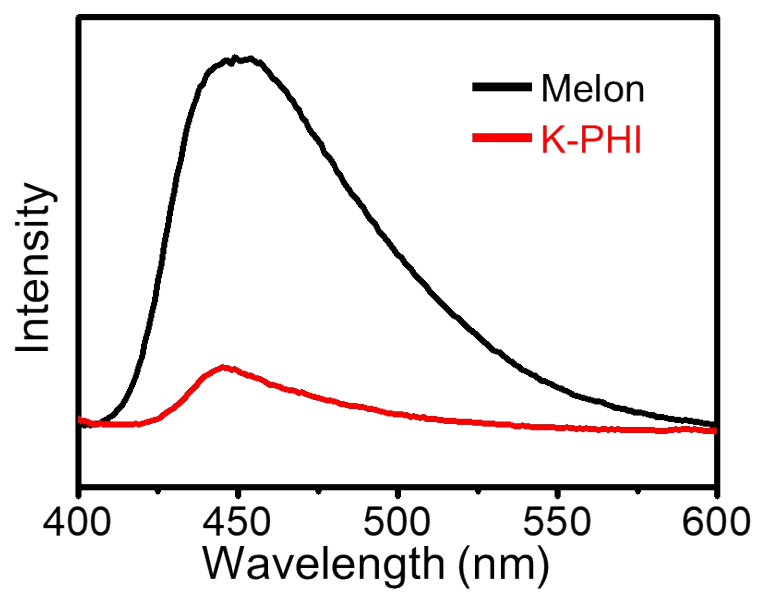


Figure S24. PL spectra of melon and K-PHI.

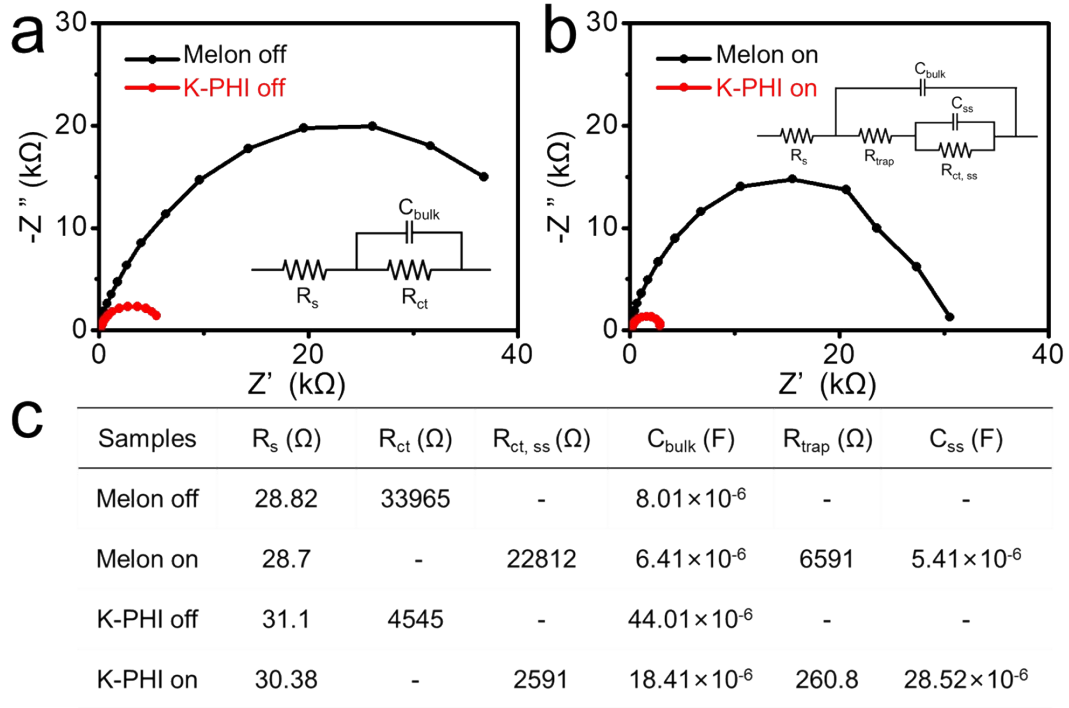


Figure S25. (a) Nyquist plots of melon and K-PHI photoanode (a) without and (b) with AM 1.5G illumination, and equivalent circuits are shown in the corresponding insets. (c) The fitting of the impedance spectrum.

Discussion

The equivalent circuit can be fitted to result series resistance (R_s), the charge transfer resistance (R_{ct}) and the space charge capacitance of the bulk (C_{bulk}) without illumination. Under illumination, we can analyze the parameters including series resistance (R_s), the charge transfer resistance from the surface to solution ($R_{ct,ss}$), the space charge capacitance (C_{bulk}), the trapping of holes in the surface states (R_{trap}) and steady state concentration of trapped holes (C_{ss}).

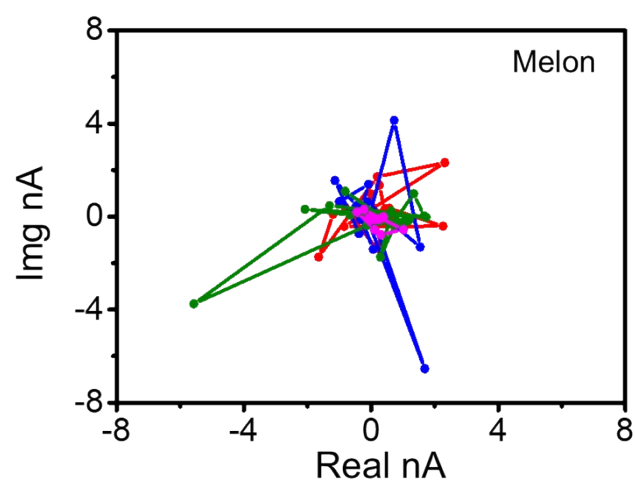


Figure S26. IMPS response of amorphous melon based photoanode.

Discussion

In IMPS, the high frequency semicircle situated in the lower quadrant refers to hole-transfer. The low frequency semicircle in the higher quadrant is relevant to surface electron-hole recombination.

Table S1. Summary of PEC performance of this work and the reported PCN-based photoanodes.

Catalyst	Precursor	Preparation method	Photocurrent density ($\mu\text{A cm}^{-2}$)	Potential vs RHE (V)	Electrolyte	Light source	Corresponding Author (Ref.)
K-PHI photoanode	Melamine and KSCN	Molten mediate polymerization	ca. 800	1.23	1.0 M NaOH	100 mW cm^{-2} , AM 1.5G (Newport)	This work
K-PHI photoanode	Melamine and KSCN	Molten mediate polymerization	ca. 550	1.23	0.1 M NaOH	100 mW cm^{-2} , AM 1.5G (Newport)	This work
CN-MR/NiFeO _x H _y electrode	Melamine, graphene oxide and Ni(NO ₃) ₂ ·6H ₂ O, etc	Doctor-blade technique assisted with CVD-like and solvothermal process	472 ± 10	1.23	0.1 M KOH	100 mW cm^{-2} , AM 1.5G (Newport)	1
CN _{TM} photoanode	Melamine and thiourea	Seeded crystallization of CN monomers assisted with CVD-like process	353	1.23	0.1 M KOH	100 mW cm^{-2} , AM 1.5G (Newport)	2
CN-MSG _{0.75} /M photoanode	Melamine, Bismuthiol and graphene oxide	Doctor-blade technique assisted with CVD-like process	270	1.23	0.1 M KOH	100 mW cm^{-2} , AM 1.5G (Newport)	3
CNP films	Melamine and cyanuric chloride	Evaporation polymerization	230	1.23	0.5 M Na ₂ SO ₄	Xe lamp, AM 1.5G	4
CN films	Melamine and formaldehyde in 2M H ₂ SO ₄	Thermal vapor condensation	228.2	1.23	0.2 M Na ₂ SO ₄	150 W Xe lamp, AM 1.5G (Newport)	5
P/B-layer-doping C ₃ N ₄ photoanode	Dicyandiamide, phosphorus acid, melamine and boric acid	Thermal vapour deposition	150 ± 10	1.23	0.1 M Na ₂ SO ₄	300 W Xe lamp, AM 1.5G	6

Table S1. (continued) Summary of PEC performance of this work and the reported PCN-based photoanodes.

Catalyst	Precursor	Preparation method	Photocurrent density ($\mu\text{A cm}^{-2}$)	Potential vs RHE (V)	Electrolyte	Light source	Corresponding Author (Ref.)
CN-MeM/M _{0.20}	Melamine	Doctor-blade technique assisted with CVD-like process	133	1.23	0.1 M KOH	100 mW cm ⁻² , AM 1.5G (Newport)	7
In situ grown porous CN/rGO films	Melamine and graphene oxide	Doctor-blade technique assisted with CVD-like process	124.5	1.23	0.1 M KOH	100 mW cm ⁻² , AM 1.5G (Newport)	8
g-CN PNR array photoanode	cyanamide	Thermal polycondensation using AAO template	120.5	1.23	0.1 M Na ₂ SO ₄	500 W Xe lamp, AM 1.5G	9
5p-PCN films	Melamine, thiourea and hexachlorocyclotri-phosphazene	Molten mediate polymerization	ca. 120	1.23	1.0 M NaOH	100 mW cm ⁻² , AM 1.5G (Newport)	10
phosphorylated PCN films	Melamine and thiourea	Molten mediate polymerization assisted with immersion method	ca. 120	1.23	1.0 M NaOH	100 mW cm ⁻² , AM 1.5G (Newport)	11
SOCN-75 films	Melamine and hydrogen peroxide solution	Thermal vapor condensation	119.2	1.23	0.1 M Na ₂ SO ₄	150 W Xe lamp, AM 1.5G (Newport)	12
CN films	Melamine	Seeded crystallization of CN monomers	116	1.23	0.1 M KOH	100 mW cm ⁻² , AM 1.5G (Newport)	13
PCN photoanode	Melamine and ammonium thiocyanate	Molten mediate polymerization	ca. 110	1.23	1.0 M NaOH	100 mW cm ⁻² , AM 1.5G (Newport)	14

Table S1. (continued) Summary of PEC performance of this work and the reported PCN-based photoanodes.

Catalyst	Precursor	Preparation method	Photocurrent density ($\mu\text{A cm}^{-2}$)	Potential vs RHE (V)	Electrolyte	Light source	Corresponding Author (Ref.)
CN-U ₁₀ M _{0.5} photoelectrode	Urea and melamine	Sprayed a seeding layer assisted with CVD-like process	ca. 110	1.23	0.1 M KOH	100 mW cm ⁻² , AM 1.5G (Newport)	15
Boron-doped CN films	Dicyandiamide and boric acid	Rapid thermal vapour deposition	103.2	1.23	0.1 M Na ₂ SO ₄	150 W Xe lamp, AM 1.5G	16
PCN films	Melamine and trithiocyanuric acid	Molten mediate polymerization	100	1.23	1.0 M NaOH	100 mW cm ⁻² , AM 1.5G (Newport)	17
Thio-CA films	Thiourea and citrate acid	Thermal vapor condensation	96.2	1.23	0.2 M Na ₂ SO ₄	150 W Xe lamp, AM 1.5G (Newport)	18
framework g-C ₃ N ₄ films	Thiourea	Thermal vapor liquid-polymerization	89	1.1	0.1 M Na ₂ SO ₄	100 mW cm ⁻² , AM 1.5G	19
DPCN/NRGO/NiFe-LDH photoanode	Urea, graphene oxide and Ni(NO ₃) ₂ ·6H ₂ O, etc	Electrophoretic deposition	72.9	1.22	0.01 M Na ₂ SO ₄	150 W Xe lamp, AM 1.5G	20
CN-rGO _{0.5} films	Melamine, cyanuric acid and graphene oxide	Doctor-blade technique	72	1.23	0.1 M KOH	100 mW cm ⁻² , AM 1.5G (Newport)	21
3%Ni-CN	Cyanuric acid, 2,4-diamino-6-phenyl-1,3,5-triazine and nickel chloride	liquid mediated pathway	69.8	1.23	0.1 M KOH	100 mW cm ⁻² , AM 1.5G (Newport)	22
CN-dicyanamide	Dicyanamide	two-step vapor	63	1.23	0.1 M	300 W Xe	23

electrode	deposition	Na ₂ SO ₄	lamp, AM 1.5G
-----------	------------	---------------------------------	------------------

Table S1. (continued) Summary of PEC performance of this work and the reported PCN-based photoanodes.

Catalyst	Precursor	Preparation method	Photocurrent density ($\mu\text{A cm}^{-2}$)	Potential vs RHE (V)	Electrolyte	Light source	Corresponding Author (Ref.)
CN-CM ₁₂₀ M electrode	Cyanuric acid and melamine	Electrophoretic deposition assisted with CVD-like process	ca. 47	1.23	0.1 M KOH	100 mW cm ⁻² , AM 1.5G (Newport)	24
CN _{MW} photoelectrode	Cyanamide	Microwave-assisted condensation	38	1.23	0.1 M KCl	150 W Xe lamp, AM 1.5G	25
CN@FTO-10%	Cyanamide	Microcontact-printing-assisted access	30.2	1.23	0.2 M Na ₂ SO ₄	500 W Xe lamp, simulated solar light source (AM 1.5G)	26
porous CN films	Melamine, cyanuric acid and barbituric acid	Doctor-blade technique	12	1.23	0.1 M KOH	100 mW cm ⁻² , AM 1.5G (Newport)	27
g-CN-50 nanorods	C and N plasma	VMFAIP system	10.8	1.23	0.5 M Na ₂ SO ₄	100 mW cm ⁻² , AM 1.5G	28
CNBC/FTO	cyanuric acid and cyanuric chloride	Solvothermal method	2	1.23	0.5 M Na ₂ SO ₄	simulated solar light source (AM 1.5G)	29

Reference

1. Karjule, N.; Singh, C.; Barrio, J.; Tzadikov, J.; Liberman, I.; Volokh, M.; Palomares, E.; Hod, I.; Shalom, M., Carbon Nitride-Based Photoanode with Enhanced Photostability and Water Oxidation Kinetics. *Adv. Funct. Mater.* **2021**, *31*, 2101724.
2. Qin, J.; Barrio, J.; Peng, G.; Tzadikov, J.; Abisdreis, L.; Volokh, M.; Shalom, M., Direct growth of uniform carbon nitride layers with extended optical absorption towards efficient water-splitting photoanodes. *Nat. Commun.* **2020**, *11* (1), 4701.
3. Karjule, N.; Barrio, J.; Xing, L.; Volokh, M.; Shalom, M., Highly Efficient Polymeric Carbon Nitride Photoanode with Excellent Electron Diffusion Length and Hole Extraction Properties. *Nano Lett.* **2020**, *20* (6), 4618-4624.
4. Jia, Q.; Zhang, S.; Gao, Z.; Yang, P.; Gu, Q., In situ growth of triazine-heptazine based carbon nitride film for efficient (photo)electrochemical performance. *Catal. Sci. Technol.* **2019**, *9* (2), 425-435.
5. Xiong, W.; Chen, S.; Huang, M.; Wang, Z.; Lu, Z.; Zhang, R. Q., Crystal-Face Tailored Graphitic Carbon Nitride Films for High-Performance Photoelectrochemical Cells. *ChemSusChem* **2018**, *11* (15), 2497-2501.
6. Luan, P.; Meng, Q.; Wu, J.; Li, Q.; Zhang, X.; Zhang, Y.; O'Dell, L. A.; Raga, S. R.; Pringle, J.; Griffith, J. C.; Sun, C.; Bach, U.; Zhang, J., Unique Layer-Doping-Induced Regulation of Charge Behavior in Metal-Free Carbon Nitride Photoanodes for Enhanced Performance. *ChemSusChem* **2020**, *13* (2), 328-333.
7. Xia, J.; Karjule, N.; Abisdreis, L.; Volokh, M.; Shalom, M., Controllable Synthesis of Carbon Nitride Films with Type-II Heterojunction for Efficient Photoelectrochemical Cells. *Chem. Mater.* **2020**, *32* (13), 5845-5853.
8. Peng, G.; Qin, J.; Volokh, M.; Liu, C.; Shalom, M., Graphene oxide in carbon nitride: from easily processed precursors to a composite material with enhanced photoelectrochemical activity and long-term stability. *J. Mater. Chem. A* **2019**, *7* (19), 11718-11723.
9. Guo, B.; Tian, L.; Xie, W.; Batool, A.; Xie, G.; Xiang, Q.; Jan, S. U.; Boddula, R.; Gong, J. R., Vertically Aligned Porous Organic Semiconductor Nanorod Array Photoanodes for Efficient Charge Utilization. *Nano Lett.* **2018**, *18* (9), 5954-5960.

-
10. Li, X.; Cheng, Z.; Fang, Y.; Fu, X.; Wang, X., In Situ Synthesis of Phosphorus-Doped Polymeric Carbon Nitride Sheets for Photoelectrochemical Water Oxidation. *Solar RRL* **2020**, *4* (8), 2000168.
 11. Fang, Y.; Li, X.; Wang, X., Phosphorylation of Polymeric Carbon Nitride Photoanodes with Increased Surface Valence Electrons for Solar Water Splitting. *ChemSusChem* **2019**, *12* (12), 2605-2608.
 12. Huang, M.; Wang, H.; Li, W.; Zhao, Y.-L.; Zhang, R.-Q., In situ textured carbon nitride photoanodes with enhanced photoelectrochemical activity by band-gap state modulation. *J. Mater. Chem. A* **2020**, *8* (45), 24005-24012.
 13. Peng, G.; Albero, J.; Garcia, H.; Shalom, M., A Water-Splitting Carbon Nitride Photoelectrochemical Cell with Efficient Charge Separation and Remarkably Low Onset Potential. *Angew. Chem. Int. Ed.* **2018**, *57* (48), 15807-15811.
 14. Fang, Y.; Li, X.; Wang, Y.; Giordano, C.; Wang, X., Gradient sulfur doping along polymeric carbon nitride films as visible light photoanodes for the enhanced water oxidation. *Appl. Catal. B* **2020**, *268*, 118398.
 15. Tashakory, A.; Karjule, N.; Abisdris, L.; Volokh, M.; Shalom, M., Mediated Growth of Carbon Nitride Films via Spray-Coated Seeding Layers for Photoelectrochemical Applications. *Adv. Sustain. Syst.* **2021**, *5*, 2100005.
 16. Ruan, Q.; Luo, W.; Xie, J.; Wang, Y.; Liu, X.; Bai, Z.; Carmalt, C. J.; Tang, J., A Nanojunction Polymer Photoelectrode for Efficient Charge Transport and Separation. *Angew. Chem. Int. Ed.* **2017**, *56* (28), 8221-8225.
 17. Fang, Y.; Li, X.; Wang, X., Synthesis of Polymeric Carbon Nitride Films with Adhesive Interfaces for Solar Water Splitting Devices. *ACS Catal.* **2018**, *8* (9), 8774-8780.
 18. Xiong, W.; Huang, M.; Huang, F.; Zhang, R.-Q., Colorful carbon nitride based composite films. *Appl. Surf. Sci.* **2020**, *511*, 145535.
 19. Lu, X.; Liu, Z.; Li, J.; Zhang, J.; Guo, Z., Novel framework g-C₃N₄ film as efficient photoanode for photoelectrochemical water splitting. *Appl. Catal. B* **2017**, *209*, 657-662.
 20. Hou, Y.; Wen, Z.; Cui, S.; Feng, X.; Chen, J., Strongly Coupled Ternary Hybrid Aerogels of N-deficient Porous Graphitic-C₃N₄ Nanosheets/N-Doped Graphene/NiFe-Layered Double Hydroxide for Solar-Driven Photoelectrochemical Water Oxidation. *Nano Lett.* **2016**, *16* (4), 2268-2277.

-
21. Peng, G.; Volokh, M.; Tzadikov, J.; Sun, J.; Shalom, M., Carbon Nitride/Reduced Graphene Oxide Film with Enhanced Electron Diffusion Length: An Efficient Photo-Electrochemical Cell for Hydrogen Generation. *Adv. Energy Mater.* **2018**, *8* (23), 1800566.
22. Zhang, W.; Albero, J.; Xi, L.; Lange, K. M.; Garcia, H.; Wang, X.; Shalom, M., One-Pot Synthesis of Nickel-Modified Carbon Nitride Layers Toward Efficient Photoelectrochemical Cells. *ACS Appl. Mater. Inter.* **2017**, *9* (38), 32667-32677.
23. Lv, X.; Cao, M.; Shi, W.; Wang, M.; Shen, Y., A new strategy of preparing uniform graphitic carbon nitride films for photoelectrochemical application. *Carbon* **2017**, *117*, 343-350.
24. Abisdris, L.; Tzadikov, J.; Karjule, N.; Azoulay, A.; Volokh, M.; Shalom, M., Electrophoretic deposition of supramolecular complexes for the formation of carbon nitride films. *Sustain. Energ. Fuels* **2020**, *4* (8), 3879-3883.
25. Zhao, T.; Zhou, Q.; Lv, Y.; Han, D.; Wu, K.; Zhao, L.; Shen, Y.; Liu, S.; Zhang, Y., Ultrafast Condensation of Carbon Nitride on Electrodes with Exceptional Boosted Photocurrent and Electrochemiluminescence. *Angew. Chem. Int. Ed.* **2020**, *59* (3), 1139-1143.
26. Liu, J.; Wang, H.; Chen, Z. P.; Moehwald, H.; Fiechter, S.; van de Krol, R.; Wen, L.; Jiang, L.; Antonietti, M., Microcontact-Printing-Assisted Access of Graphitic Carbon Nitride Films with Favorable Textures toward Photoelectrochemical Application. *Adv. Mater.* **2015**, *27* (4), 712-718.
27. Peng, G.; Xing, L.; Barrio, J.; Volokh, M.; Shalom, M., A General Synthesis of Porous Carbon Nitride Films with Tunable Surface Area and Photophysical Properties. *Angew. Chem. Int. Ed.* **2018**, *57* (5), 1186-1192.
28. Wang, R.; Liu, H.; Fan, Z.; Li, L.; Cai, Y.; Xu, G.; Luo, W.; Yang, B.; Zhou, Y.; Zou, Z., Unconventional gas-based bottom-up, meter-area-scale fabrication of hydrogen-bond free g-CN nanorod arrays and coupling layers with TiO₂ toward high-efficiency photoelectrochemical performance. *Nanoscale* **2018**, *10* (7), 3342-3349.
29. Gu, Q.; Gong, X.; Jia, Q.; Liu, J.; Gao, Z.; Wang, X.; Long, J.; Xue, C., Compact carbon nitride based copolymer films with controllable thickness for photoelectrochemical water splitting. *J. Mater. Chem. A* **2017**, *5* (36), 19062-19071.